Tuning the metal-support interaction in catalysts for highly efficient methane dry reforming reaction

Fagen Wang [a,b,*], Leilei Xu [b], Jian Zhang [b], Yu Zhao [c], Hui Li [c], He Xing Li [c], Kai Wu [d,e], Guo Qin Xu [a,b,d,*], Wei Chen [a,b,d,f,*]

[a] Laboratory of Energy and Environment Interface Engineering, National University of Singapore Suzhou Research Institute, 377 Linquan Street, Suzhou 215123, China
[b] Department of Chemistry, National University of Singapore, 3 Science Drive 3, 117543, Singapore
[c] Department of Chemistry, Shanghai Normal University, Shanghai 200234, PR China
[d] Singapore-Peking University Research Centre for a Sustainable Low-Carbon Future, 1CREATE Way, #15-01 CREATE Tower, 138602, Singapore
[e] BNLMS, SKLSCUSS, College of Chemistry and Molecular Engineering, Peking University, Beijing 100871, PR China
[f] Department of Physics, National University of Singapore, 2 Science Drive 3, 117543, Singapore

ARTICLE INFO

ABSTRACT

The metal-support interaction of Ir/Ce$_{0.9}$Pr$_{0.1}$O$_2$ catalyst is tuned by adopting different preparation techniques of deposition–precipitation (DP), co-precipitation (CP) and sequential precipitation (SP) to control the locations of Ir, improving catalytic performance in methane dry reforming reaction. Ir/Ce$_{0.9}$Pr$_{0.1}$O$_2$-DP catalyst shows the highest catalytic performance and stability due to the unembedded Ir nanoparticles on catalyst surfaces, followed by Ir/Ce$_{0.9}$Pr$_{0.1}$O$_2$-SP and Ir/Ce$_{0.9}$Pr$_{0.1}$O$_2$-CP catalysts in which Ir species are either partially or fully embedded in Ce-Pr-O mixed oxides. Our results clearly demonstrate that the metal-support interaction plays important roles in controlling the catalyst sintering and carbonaceous deposition.

© 2015 Elsevier B.V. All rights reserved.

1. Introduction

Although fossil fuels provide more than 80% of global energy resources, their non-sustainable and non-renewable nature may limit the future economic development. The predictable fossil fuels depletion calls for great efforts to explore innovative and more efficient ways in using this natural resource. As one of the largest reserves on Earth, methane can be converted to syngas and C$_2$ hydrocarbons through steam reforming, partial oxidation and oxidative coupling [1]. Owing to the strong bond strength of C—H (434 kJ/mol), the activation of methane requires high temperature, implying a high energy input [2]. Thus methane utilization and conversion at a relatively low temperature becomes a great challenge and a hot topic for research.

On the other hand, the combustion of fossil fuels produces abundant CO$_2$, which contributes to global warming. Reducing CO$_2$ emission has been receiving much attention in recent years. One approach is carbon capture and sequestration, and the other is CO$_2$ transformation into value-added chemicals [3]. For the latter, dry reforming of methane (DRM) represents one promising way to simultaneously convert greenhouse gases of methane and CO$_2$ to syngas, which can further be used as feedstock for long chain hydrocarbons production through Fischer–Tropsch synthesis [4].

Great efforts have been devoted to developing catalysts for DRM, mainly consisting of transition and noble metals [1,4–9]. Among these metals, Ni catalyst shows high performance for methane conversion due to its excellent C—H breaking capacity. However, severe coke formation and Ni nanoparticles sintering were found to cause catalyst deactivation [10]. The size of Ni nanoparticles was reported to have a significant effect on the coke formation. Small Ni nanoparticles (<5 nm) were recently synthesized for DRM to minimize coke [11]. Noble metal catalysts exhibit a better performance for DRM reaction compared to Ni catalysts [12,13]. Under the conditions of stoichiometric feedstock and atmospheric pressure, high conversions of methane and CO$_2$ were achieved over Ru, Rh, and Ir [11]. Although the noble metal catalysts are used for DRM, the supports of catalysts were found to be critical in coke formation. Heavy coke deposition was observed on irreducible oxides [14,15], while much less extent was seen on reducible oxides [9,16].

---

* Corresponding authors at: Laboratory of Energy and Environment Interface Engineering, National University of Singapore Suzhou Research Institute, 377 Linquan Street, Suzhou 215123, China. Fax: +65 6779 1691.
E-mail addresses: fagen.wang@gmail.com (F. Wang), chmxugq@nus.edu.sg (G.Q. Xu), chmcw@nus.edu.sg (W. Chen).

In literatures [1,9,17], the bi-functional mechanism is well accepted for DRM over catalysts supported on the reducible oxides. Methane is activated on the active metal to form adsorbed H and CH_x intermediates while CO_2 binds on the support to produce carbonates or dissociate into CO and O. The CH_x intermediates react with the carbonates or the dissociated O at the metal-support boundaries, resulting in CO and formate species. The formate is subsequently decomposed to CO and OH group, which further reacts with the CH_x to yield CO and H_2. From this reaction pathway, it is clear that the properties of active metals and supports, and their synergies are vital for DRM catalytic performances. Noble metals like Pt and Ir were shown to be highly active in methane activation [16,17]. Ceria and ceria-based mixed oxides are excellent support candidates for CO_2 activation through oxygen vacancies. These supports like CeO_2, $Ce_{1-x}Zr_xO_{2-\delta}$ and $Ce_{1-x}Pr_xO_{2-\delta}$ have abilities to store and release oxygen (oxygen storage capacity, OSC) [18–20], which is very beneficial for coke gasification [20]. The interaction between metal and ceria not only promotes OSC to further coke elimination [10], and also strengthens catalyst structure to mitigate sintering of active metal [21]. Therefore, the coupling of noble metals with ceria-based mixed oxides may allow us to design promising catalysts for DRM [20,22,23].

In our previous study, it was found that $Ir/Ce_{0.9}Pr_{0.1}O_2$ catalyst greatly enhanced the activity and stability for high temperature ethanol steam reforming reaction, which was contributed from the doping of PrO_x promoted the redox property of ceria by creating more surface oxygen vacancies and improved the thermal stability of ceria by partially avoiding sintering. Considering the high reaction temperature and the similar causes for catalysts deactivation in ethanol steam reforming and DRM reactions, $Ir/Ce_{0.9}Pr_{0.1}O_2$ catalysts were synthesized to develop highly efficient catalysts for DRM reaction in this work. It is wished that the enhanced OSC would reduce coke deposition and the promoted metal-support interaction might prevent active metal sintering. The metal-support interaction was tuned by different preparation methods to position Ir species at different locations in the catalysts. It was revealed that the highest conversions of methane and carbon dioxide reached 60% and 75%, respectively, at a space velocity of 18,000 mL/(gh) over the catalyst prepared by deposition precipitation. The performance was maintained for at least 200 h at 1023 K. No obvious coke deposits and Ir sintering can be found on the used samples.

2. Experimental

2.1. Catalysts preparation

$Ir/Ce_{0.9}Pr_{0.1}O_2$-DP catalyst (noted as Ir/CePr-DP) was synthesized by deposition–precipitation (DP). A homogeneous mixture of $CO(NH_2)_2$ (2.08 mol/L), $Ce(NO_3)_3$ (0.040 mol/L) and $Pr(NO_3)_3$ (0.0044 mol/L) was heated to 363 K and stirred for 5 h. After filtration and washing, the precipitates were dried at 373 K overnight and calcined at 673 K for 4 h to form $Ce_{0.9}Pr_{0.1}O_2$-DP support. This support (1.0 g) was mixed with H_2IrCl_6 solution (0.0078 mol/L, 14 mL) in 400 mL water at 338 K, followed by dropping Na_2CO_3(aq., 0.20 mol/L, 100 mL). After filtration and washing, the powders were dried at 373 K overnight and calcined at 1023 K for 4 h.

$Ir/Ce_{0.9}Pr_{0.1}O_2$-CP catalyst (noted as Ir/CePr-CP) was prepared by co-precipitation (CP). A mixture of $Ce(NO_3)_3$ (0.040 mol/L), $Pr(NO_3)_3$ (0.044 mol/L) and H_2IrCl_6 (8.54×10^{-4} mol/L) was gradually added to Na_2CO_3 (aq., 0.2 mol/L, 300 mL) at 338 K under vigorous stirring. After aged for 3 h, the precipitate was filtrated and washed. The obtained powders were dried at 373 K overnight and calcined at 1023 K for 4 h. $Ce_{0.9}Pr_{0.1}O_2$-CP support was prepared in the same way without H_2IrCl_6.

$Ir/Ce_{0.9}Pr_{0.1}O_2$-SP catalyst (noted as Ir/CePr-SP) was synthesized by sequential precipitation (SP). First, Na_2CO_3(aq., 0.2 mol/L,

100 mL) was dropped to a mixture of $Ce(NO_3)_3$ (0.040 mol/L) and $Pr(NO_3)_3$ (0.0044 mol/L) at 338 K. Then, H_2IrCl_6 (0.0078 mol/L, 44 mL) was added and precipitated. After the suspension was filtrated, the obtained solid was dried at 373 K overnight and calcined at 1023 K for 4 h. $Ce_{0.9}Pr_{0.1}O_2$-SP support preparation was followed the same method without H_2IrCl_6.

2.2. Catalyst characterizations

The actual Ir loadings were analyzed by inductively coupled plasma atomic emission spectrometry (ICP-AES). Nitrogen adsorption–desorption isotherms were measured using a surface area and pore size analyzer (NOVA 2200e) at 77 K. Before the measurement, samples were degassed at 573 K for 3 h. The surface area was obtained with a multipoint BET analysis of the nitrogen adsorption isotherm.

X-ray diffraction (XRD) patterns of the samples were recorded using a PANalytical Empyren DY 708 diffractometer with Cu radiation (Cu Kα = 0.15406 nm). The mean crystalline size was calculated based on the Scherrer equation.

Transmission electron microscopy (TEM) images were taken using JEOL 2010 operated at 200 kV. Specimens were prepared by ultrasonically suspending samples in ethanol. Droplets of the suspension were deposited on a thin carbon film supported on a standard copper grid.

X-ray photoelectron spectra (XPS) were recorded with an AMI-CUS spectrometer using Mg Ka radiation. The charging effect was corrected by referencing the binding energy of C 1s at 284.6 eV. The spectra curves of Pr and Ir species were fitted using a Gaussian procedure due to the weak intensities and low contents, while raw data were used for the spectra of O, Ce and C.

Hydrogen temperature programmed reduction (H_2-TPR) of fresh samples was conducted in a U-shaped reactor connected to a mass spectrometer (PrismaPlus). 100 mg samples were loaded and pretreated under flowing He (50 mL/min) at 573 K for 1 h. After cooling down at room temperature, a mixture of 10%H_2/He (50 mL/min) was introduced through the samples to reach a steady state. The temperature was then increased to 1023 K at a rate of 5 K/min and the signal of H_2 (m/e = 2) was monitored by the mass spectrometer.

CO_2 temperature programmed desorption (CO_2-TPD) was performed in the U-shaped reactor. The samples were pretreated by 10%H_2/He (20 mL/min) at 673 K for 30 min. 5% CO_2/He (20 mL/min) was then passed through at room temperature for 30 min. After purged by He (20 mL/min), the samples were heated to 1023 K with a rate of 5 K/min and the signal of CO_2 (m/e = 44) was monitored by the mass spectrometer (PrismaPlus).

CH_4 temperature programmed surface reaction (CH_4-TPSR) was carried out in the U-type reactor. Fresh samples were reduced by 10%H_2/He (20 mL/min) at 673 K for 30 min. After temperature was cooled down, 5% CH_4/He (20 mL/min) was introduced to a stable state. Then the samples were heated to 1073 K at a rate of 5 K/min. The signals of CO_2 (m/e = 44), H_2O (m/e = 18), CH_4 (m/e = 15), CO (m/e = 28) and H_2 (m/e = 2) were measured.

$CH_4 + CO_2$ temperature programmed surface reaction (TPSR of $CH_4 + CO_2$) was run in the U-type reactor. Firstly, samples were heated to 673 K for reduction 30 min, and were treated by 5% CO_2/He (20 mL/min) at room temperature for 30 min. Then, 5%CH_4/He (20 mL/min) was switched to the samples. After CO_2 was purged, temperature was increased to 1073 K at 5 K/min. The signals of CO_2 (m/e = 44), H_2O (m/e = 18), CH_4 (m/e = 15), CO (m/e = 28) and H_2 (m/e = 2) were recorded.

Temperature programmed oxidation (TPO) of used catalysts was conducted in the U-type reactor. The used samples were initially heated to 573 K for 30 min under flowing He to eliminate possible contaminants. The samples were then heated from room
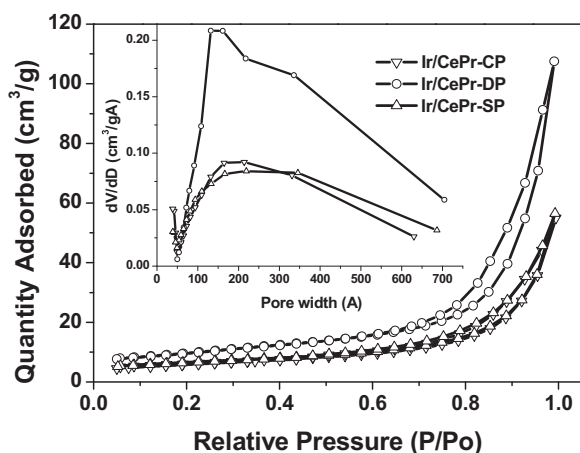
Fig. 1. Nitrogen adsorption–desorption isotherms and BJH desorption pore distributions of fresh Ir/Ce$_{0.9}$Pr$_{0.1}$O$_2$-CP, Ir/Ce$_{0.9}$Pr$_{0.1}$O$_2$-DP, and Ir/Ce$_{0.9}$Pr$_{0.1}$O$_2$-SP catalysts.

temperature to 1073 K under 5%O$_2$/He (50 mL/min). The effluent composition CO$_2$ (m/e = 44) was monitored by the mass spectrometer (PrismaPlus).

2.3. Catalytic activity tests

DRM reaction was performed in a fixed-bed reactor. Before the reaction, 100 mg fresh catalyst was reduced by 20%H$_2$/N$_2$ (30 mL/min) at 1023 K for 1 h. Upon purging the reactor by N$_2$ (24 mL/min) and decreasing the temperature to 873 K, a mixture of undiluted CH$_4$ and CO$_2$ (molar ratio CH$_4$/CO$_2$ = 1) was introduced at a gas hourly space velocity (GHSV) of 18,000 mL/(gh). Catalytic performance was measured from 873 K to 1023 K at an interval of 50 K. The effluents in the outlet were separated by a packed column (TDX-01) and analyzed by an on-line gas chromatography (Agilent 7890A). The conversions of CH$_4$ and CO$_2$ were determined from the corresponding flow rates in the inlet and outlet streams.

3. Results and discussion

3.1. Physical and chemical properties of the fresh Ir/Ce$_9$Pr$_{0.1}$O$_2$ catalysts

#### 3.1.1. Physical characterizations of the fresh Ir/Ce$_9$Pr$_{0.1}$O$_2$ catalysts

Fig. 1 shows the N$_2$ adsorption/desorption isothermal plots of fresh Ir/Ce$_{0.9}$Pr$_{0.1}$O$_2$ catalysts prepared by different techniques.

All the catalysts exhibit the type-IV isotherm curves. The BET specific areas of the Ir/Ce$_{0.9}$Pr$_{0.1}$O$_2$-CP, Ir/Ce$_{0.9}$Pr$_{0.1}$O$_2$-DP and Ir/Ce$_{0.9}$Pr$_{0.1}$O$_2$-SP catalysts were 21, 34 and 23 m^2/g, respectively. The corresponding average pore volumes of the catalysts were 0.089, 0.174 and 0.090 cm^3/g, and the average pore diameters of the catalysts were 16.1, 19.5 and 15.5 nm. The real Ir loadings by ICP are 2.05, 2.01 and 1.96 wt.% for the catalysts of Ir/Ce$_{0.9}$Pr$_{0.1}$O$_2$-CP, Ir/Ce$_{0.9}$Pr$_{0.1}$O$_2$-DP and Ir/Ce$_{0.9}$Pr$_{0.1}$O$_2$-SP, respectively.

Fig. 2A shows the XRD patterns of the catalysts. For mixed oxides, main diffraction peaks of CeO$_2$ (PDF#34-0394) with fluorite structure were observed. The absence of peaks from Pr$_6$O$_{11}$ species suggests the solid solution formation of Ce-Pr-O oxides. The mixed oxides are about 17, 14 and 13 nm with lattice parameters of 5.4098, 5.4107 and 5.4172 Å for the Ir/Ce$_{0.9}$Pr$_{0.1}$O$_2$-DP, Ir/Ce$_{0.9}$Pr$_{0.1}$O$_2$-CP and Ir/Ce$_{0.9}$Pr$_{0.1}$O$_2$-SP catalysts, respectively. The marginally increased lattice parameters compared to pure ceria (5.4051 Å) is possibly due to the doping of Pr^{3+} (ionic radii: 101.3 pm) into the matrix of ceria (Ce^{4+} ionic radii: 92 pm) that causes a slight expansion [20], which causes the (1 1 1) diffraction peak of mixed oxides shift toward a lower angle compared to that of CeO$_2$ (Fig. 2B). In regard to Ir species, no diffraction peak was detected on the Ir/Ce$_{0.9}$Pr$_{0.1}$O$_2$-CP and Ir/Ce$_{0.9}$Pr$_{0.1}$O$_2$-SP catalysts, indicating that the Ir species are highly dispersed or too small to be measured. In contrast, the diffraction peak of IrO$_2$ with a size of 5∼6 nm was evidenced in the case of the Ir/Ce$_{0.9}$Pr$_{0.1}$O$_2$-DP catalyst.

The morphology images of the Ir/Ce$_{0.9}$Pr$_{0.1}$O$_2$ samples are illustrated in Fig. 3. Irregular polyhedron nanoparticles of Ce-Pr-O mixed oxides in the range of 10–15 nm are presented and oriented randomly. The lattice inter-planar spacing of 0.312 nm corresponds to the most favorable (1 1 1) crystal face of ceria. As to the Ir species, IrO$_2$ nanoparticles (5∼6 nm, inter-plane spacing of 0.158 nm) were found on the surface of the Ir/Ce$_{0.9}$Pr$_{0.1}$O$_2$-DP catalyst, whereas they were hardly observed on the Ir/Ce$_{0.9}$Pr$_{0.1}$O$_2$-CP and Ir/Ce$_{0.9}$Pr$_{0.1}$O$_2$-SP catalysts. These observations are in good agreement with the above XRD measurements.

Fig. 4 shows the results of XPS spectra. The Ce 3d spectra (Fig. 4A) comprises of eight peaks, corresponding to four pairs of spin-orbital splitting doublets. The spectra of Pr 3d (Fig. 4B) exhibits two sets of peaks with binding energies of 952.7 and 932.7 eV assigned to Pr^{4+}, and 947.3 and 927.3 eV attributed to Pr^{3+} [20]. This demonstrates the co-existences of Pr^{4+} and Pr^{3+} in the mixed oxides, in which the latter causes the lattice expansion as discussed in XRD. The O 1s profile gives two binding energies at 531.1 and 528.5 eV (Fig. 4C), related to oxygen species of defects (noted as Oβ) and lattice oxygen (noted as Oα) [24], respectively. The higher Oβ concentration in the Ir/Ce$_{0.9}$Pr$_{0.1}$O$_2$-DP catalyst (Table 1) affirms the richness of oxygen defects. The Ir 4f spectra (Fig. 4D) show a doublet at 61.6 and 64.5 eV, indicative of IrO$_2$ species. It should be noted that the
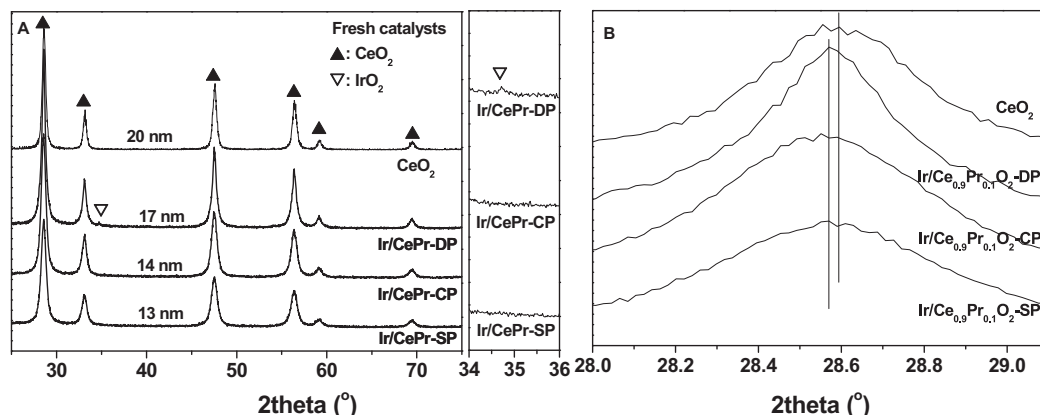
Fig. 2. XRD patterns of the fresh Ir/Ce$_{0.9}$Pr$_{0.1}$O$_2$ catalysts.
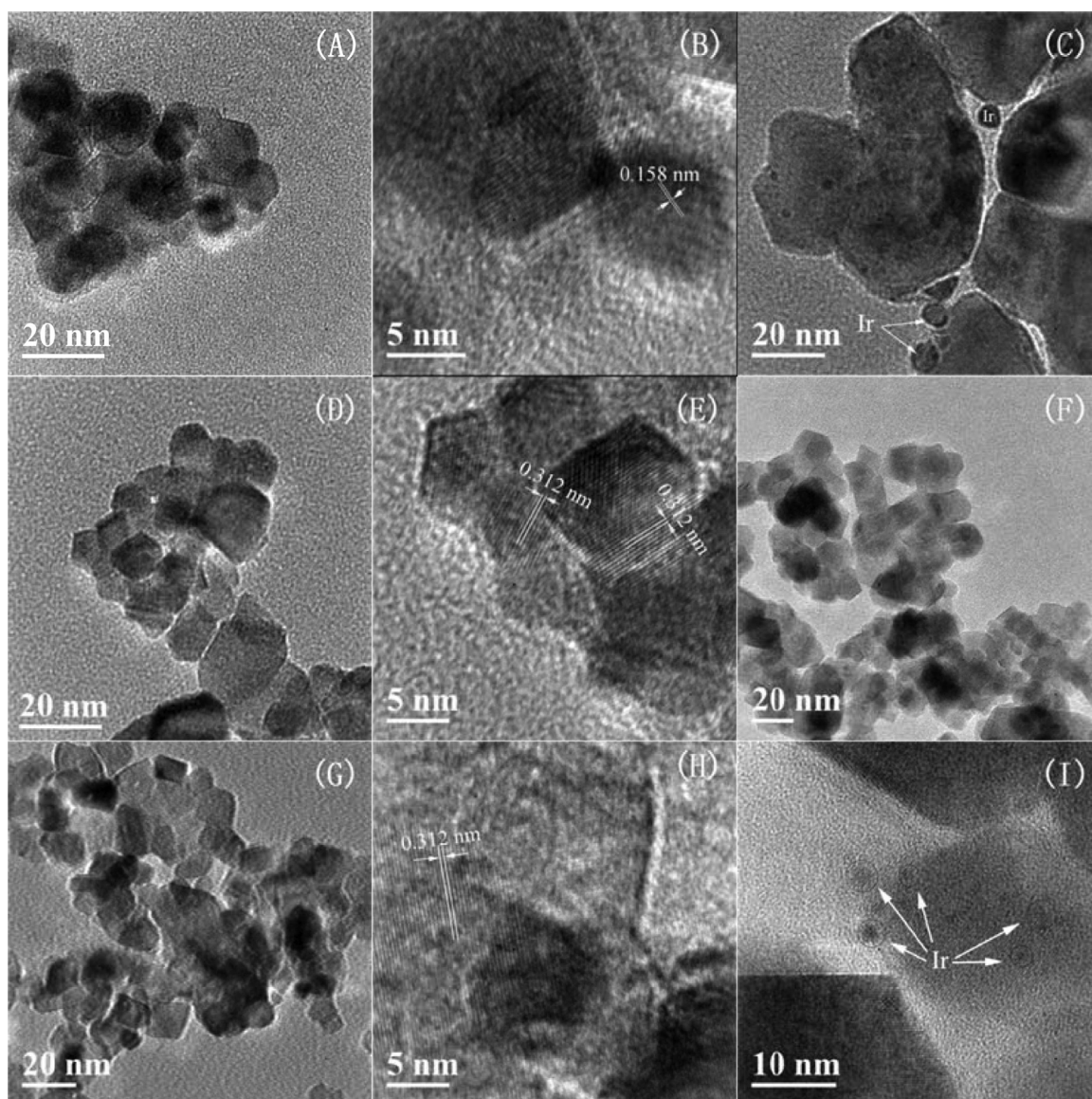
Fig. 3. The TEM images of fresh $Ir/Ce_{0.9}Pr_{0.1}O_2$-DP (A and B), $Ir/Ce_{0.9}Pr_{0.1}O_2$-CP (D and E), $Ir/Ce_{0.9}Pr_{0.1}O_2$-SP (G and H) catalysts and reduced $Ir/Ce_{0.9}Pr_{0.1}O_2$-DP (C), $Ir/Ce_{0.9}Pr_{0.1}O_2$-CP (F), $Ir/Ce_{0.9}Pr_{0.1}O_2$-SP (I).

Ir 4f spectra of the $Ir/Ce_{0.9}Pr_{0.1}O_2$-CP catalyst shows a down-shift. This might indicate discrepant chemical conditions of Ir species. We propose that the Ir species were embedded in the Ce-Pr-O mixed oxide and formed a chemical bond.

3.1.2. Chemical properties of the fresh $Ir/Ce_9Pr_{0.1}O_2$ catalysts

Fig. 5 displays H_2-TPR profiles of catalysts. For the mixed oxides (Fig. 5A), surface oxygen reductions are centered at 887 K, 945 K and 933 K for samples prepared by DP, CP and SP, respectively

Table 1
Surface weight compositions, OSCs and texture properties of the Ir catalysts.

Samples	Surface composition (wt.%)				$O\beta$ (%)	Ce^{3+} (%)	Pr^{3+} (%)	OSC (μmol O/g_{cat})	BET (m^2/g)	Pore volume (cm^3/g)	Pore size (nm)	Sintering degree
	Ce	Pr	Ir	O								
$Ce_{0.9}Pr_{0.1}O_2$-DP	34.0	21.3	–	15.5	7.5	9.2	8.3	389	–	–	–	–
$Ce_{0.9}Pr_{0.1}O_2$-CP	39.5	27.0	–	18.7	11.5	13.5	15.3	454	–	–	–	–
$Ce_{0.9}Pr_{0.1}O_2$-SP	41.2	22.8	–	13.9	5.9	12.1	10.8	410	–	–	–	–
Fresh $Ir/Ce_{0.9}Pr_{0.1}O_2$-DP	48.9	13.4	2.4	30.2	13.4	18.7	6.0	860	34.2	0.17	19.5	–
Fresh $Ir/Ce_{0.9}Pr_{0.1}O_2$-CP	56.3	11.5	1.3	23.8	11.4	18.2	3.4	997	21.1	0.09	16.1	–
Fresh $Ir/Ce_{0.9}Pr_{0.1}O_2$-SP	51.2	24.2	2.0	16.5	9.6	15.8	12.1	906	22.6	0.09	15.5	–
Used $Ir/Ce_{0.9}Pr_{0.1}O_2$-DP	35.8	16.5	2.2	23.6	10.1	6.9	7.1	–	5.7	0.08	51.3	82%
Used $Ir/Ce_{0.9}Pr_{0.1}O_2$-CP	39.9	20.6	1.5	19.5	5.0	10.2	8.7	–	4.9	0.03	22.3	114%
Used $Ir/Ce_{0.9}Pr_{0.1}O_2$-SP	37.8	15.2	2.1	19.5	8.2	9.2	7.2	–	5.2	0.07	31.7	107%

Note: not measured or not available; sintering degree = (crystalline size of mixed oxide in the used sample − crystalline size of mixed oxide in the fresh sample)/(crystalline size of mixed oxide in the fresh sample).
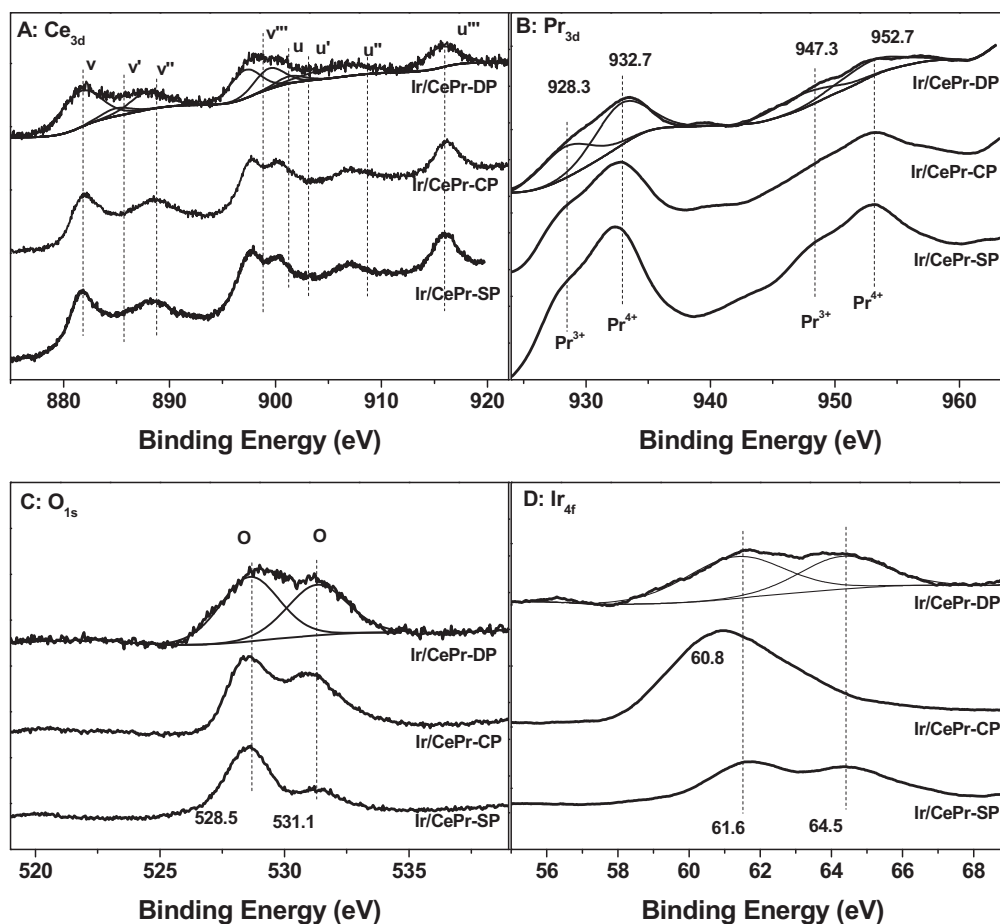
Fig. 4. XPS profiles of Ce_{3d} (A), Pr_{3d} (B), O_{1s} (C) and Ir_{4f} (D) of the fresh $Ir/Ce_{0.9}Pr_{0.1}O_2$ catalysts.

[25]. The temperature differences may be associated with different solid solution degrees of Ce-Pr-O that results in different surface oxygen reactivity with hydrogen [25,26]. The removal of bulk oxygen will occur at temperatures above 1168 K [26], which is beyond our heating system. After loading Ir species, the redox of catalysts is enhanced (Fig. 5B). The co-reductions of Ir species and partial surface oxygen of oxides occur at 600 K, 662 K and 625 K for the $Ir/Ce_{0.9}Pr_{0.1}O_2$-DP, $Ir/Ce_{0.9}Pr_{0.1}O_2$-CP and $Ir/Ce_{0.9}Pr_{0.1}O_2$-SP catalysts, respectively. The further surface oxygen removal of oxides were observed at 805 K and 842 K for the catalysts prepared by DP and CP [27], but not present for the catalyst prepared by SP. This indicates that the surface oxygen reduction is almost complete at 623 K for the $Ir/Ce_{0.9}Pr_{0.1}O_2$-SP catalyst, which can also be derived from its larger area of hydrogen consumption compared to the other two catalysts. From the above, it is suggested that the $Ir/Ce_{0.9}Pr_{0.1}O_2$-DP catalyst shows the highest redox property owing to the lowest reduction temperatures of Ir species and surface oxygen of oxides. The nature of preparation methods might account for this. In the DP method, all $Ir(OH)_4$ species are deposited on the $Ce_{0.9}Pr_{0.1}O_2$-DP support surfaces by slow addition of Na_2CO_3 [28]. Such unembedded Ir species favors the low temperature reduction due to the metal-support interaction. During the SP procedure, Ce^{3+} and Pr^{3+} are sequential precipitated to $Ce(OH)_3$ and $Pr(OH)_3$ mixed nanoparticles, followed by the deposition of $Ir(OH)_4$ species. In the calcination treatment, both Pr^{3+} species and partial Ir^{4+} species would enter into the bulk of ceria due to the adsorption capacity of ceria, causing the Ir species to be partially embedded in Ce-Pr-O mixed oxide [29]. This is consistent with its intermediate reduction temperature due to the stronger metal-support interaction. In

the CP approach, species of Ir^{4+}, Ce^{3+} and Pr^{3+} are co-precipitated. Thus, Pr^{3+} and Ir^{4+} are present in the bulk phase of ceria to form Ce-Pr-Ir-O composite after calcination. This chemically embedded Ir species (discussed in the XPS profile) leads to the highest reduction temperature due to the strongest metal-support interaction [29].

The metal-support interaction is further evidenced by the oxygen storage capacities. In Table 1, the OSCs were measured about 389, 454 and 410 μmol O/g for the mixed oxides prepared by DP, CP and SP, respectively. These values were enhanced to 860, 997 and 906 μmol O/g after Ir loading on the corresponding catalysts. The orders of increased OSCs are in line with that of the metal-support interaction, demonstrating the promotion effect of noble metal on the OSC of support [30].

3.2. Dynamic reaction analysis of DRM over the $Ir/Ce_9Pr_{0.1}O_2$ catalysts

3.2.1. CO_2-TPD

Fig. 6 shows the CO_2-TPD profiles of the catalysts to analyze CO_2 activation. CO_2 peaks, located at about 380–420 K, 577–628 K and 741–762 K, are identified during the desorption process. These can be correlated with different carbonaceous species. The peak around 380–420 K could be assigned to the reactive bicarbonates resulting from the interactions of CO_2 with hydroxyl groups on the support surfaces[31]. The peak within 577–628 K might be attributed to the more stable carbonates from the interactions of CO_2 with surface oxygen atoms of the mixed oxides. The peak of 741–765 K is possibly related to the structural carbonates coming from the
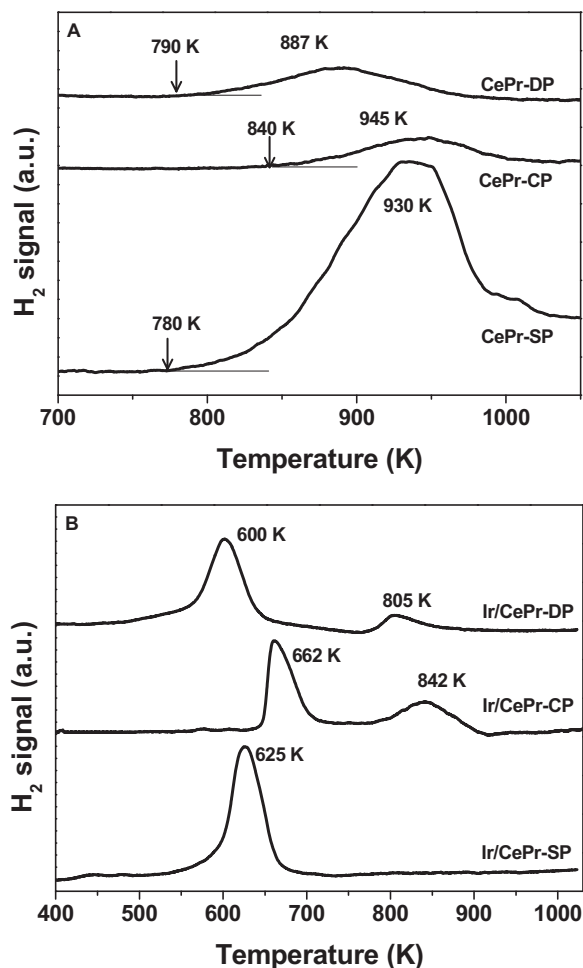
Fig. 5. TPR profiles of (A) $Ce_{0.9}Pr_{0.1}O_2$ supports and (B) fresh $Ir/Ce_{0.9}Pr_{0.1}O_2$ catalysts.
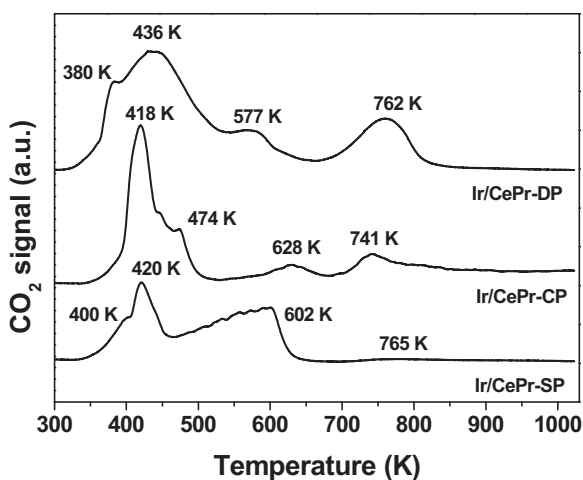

Fig. 6. CO_2-TPD profiles of the $Ir/Ce_{0.9}Pr_{0.1}O_2$ catalysts.

reaction of bulk oxygen with CO_2 [27,32]. By analyzing the normalized percentages and CO_2 desorption areas of carbonaceous species (Table 2), it is concluded that the $Ir/Ce_{0.9}Pr_{0.1}O_2$-DP catalyst exhibits the most carbonates species, suggesting the strongest interaction between CO_2 and $Ce_{0.9}Pr_{0.1}O_2$-DP support.

Table 2
Area comparisons of CO_2 desorption of the $Ir/Ce_{0.9}Pr_{0.1}O_2$ catalysts after reduction.

	$Ir/Ce_{0.9}Pr_{0.1}O_2$-DP	$Ir/Ce_{0.9}Pr_{0.1}O_2$-CP	$Ir/Ce_{0.9}Pr_{0.1}O_2$-SP
380–420 K	0.710	0.815	0.424
577–628 K	0.107	0.055	0.561
741–765 K	0.183	0.134	0.025
Total area (a.u.)	4.23e-10	2.26e-10	2.51e-10

3.2.2. CH_4-TPSR

Fig. 7 displays the results of CH_4-TPSR to analyze CH_4 interaction with catalysts and discuss the roles of oxygen species. Below 900 K, methane consumption peaks were observed at 650 K and 730 K for $Ir/Ce_{0.9}Pr_{0.1}O_2$-DP, 778 K for $Ir/Ce_{0.9}Pr_{0.1}O_2$-SP and 855 K for $Ir/Ce_{0.9}Pr_{0.1}O_2$-CP catalyst. Originated from methane cracking, hydrogen starts to desorb at 690 K, 775 K and 873 K over $Ir/Ce_{0.9}Pr_{0.1}O_2$-DP, $Ir/Ce_{0.9}Pr_{0.1}O_2$-SP and $Ir/Ce_{0.9}Pr_{0.1}O_2$-CP catalysts, respectively. Furthermore, minor CO_2 peaks were detected at 652 K, 792 K and 858 K, followed by minor H_2O peaks detected at 700 K, 800 K and 860 K over the corresponding catalysts. This result implies that the CH_x intermediates would react with surface oxygen of the mixed oxides at the metal-support boundaries: $CH_x (x < 4) + CeO_2 \rightarrow CeO_\delta (1.5 < \delta < 2) + CO_2 + H_2O$ [33]. Above 900 K, CO_2 was almost unavailable, but methane continues to be consumed to produce $H_2 + CO$ through the reaction between CH_x and bulk oxygen of the mixed oxides: $CH_x (x < 4) + CeO_2 \rightarrow CeO_\delta (1.5 < \delta < 2) + CO + H_2$ [33]. This result demonstrates the ability of oxygen species in ceria-based mixed oxides in eliminating coke precursors at perimeters.

3.2.3. TPSR of $CH_4 + CO_2$

Fig. 8 shows the TPSR results of $CH_4 + CO_2$. Methane consumption peaks were observed at 660 K and 1000 K for the $Ir/Ce_{0.9}Pr_{0.1}O_2$-DP, 960 K for the $Ir/Ce_{0.9}Pr_{0.1}O_2$-SP and 955 K for the $Ir/Ce_{0.9}Pr_{0.1}O_2$-CP. The much higher consumption temperatures compared to those in the above CH_4-TPSR could be due to the different electronic surroundings of Ir nanoparticles, influenced by the pre-adsorbed CO_2. Hydrogen was released from 690 K, 805 K and 940 K over the $Ir/Ce_{0.9}Pr_{0.1}O_2$-DP, $Ir/Ce_{0.9}Pr_{0.1}O_2$-SP and $Ir/Ce_{0.9}Pr_{0.1}O_2$-CP catalysts, respectively. CO_2 desorption at 400 K was assigned to the weak carbonate species interacting with supports as discussed in CO_2-TPD process. Besides, a small CO_2 peak was found at 665 K for the $Ir/Ce_{0.9}Pr_{0.1}O_2$-DP, 840 K for the $Ir/Ce_{0.9}Pr_{0.1}O_2$-SP and 960 K for the $Ir/Ce_{0.9}Pr_{0.1}O_2$-CP catalyst, followed by minor H_2O at 680 K, 830 K and 970 K over the corresponding catalysts. These were considered from the reaction of methane with the surface oxygen of mixed oxides. Above 1000 K, CO and hydrogen were monitored as the main products, revealing the reaction between methane and the bulk oxygen of mixed oxides.

3.3. Roles of oxygen species and proposed DRM mechanism over the $Ir/Ce_9Pr_{0.1}O_2$ catalysts

From the above results, including CO_2-TPD, CH_4-TPSR and TPSR of $CH_4 + CO_2$, the roles of oxygen species over the $Ir/Ce_{0.9}Pr_{0.1}O_2$ catalysts for DRM are tentatively analyzed: the surface oxygen species promotes methane oxidation to CO_2 and H_2O at temperatures below 900 K, and the bulk oxygen species facilitates methane conversion to syngas at temperatures above 900 K. The reaction pathways of DRM are attempted to be proposed basing on the above dynamics and bi-functional mechanism in references [1,34,35]. Carbon dioxide adsorbs on the mixed oxide to form carbonaceous intermediates or dissociates to produce CO and oxygen species. Methane is activated at the Ir metallic sites to form CH_x which diffuses to the boundary between Ir and mixed oxide as the tem-
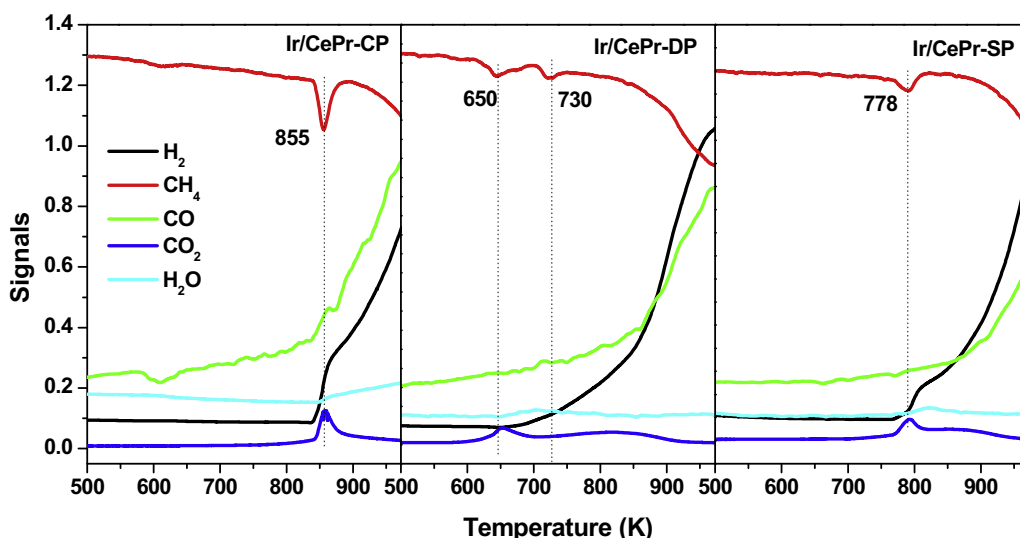
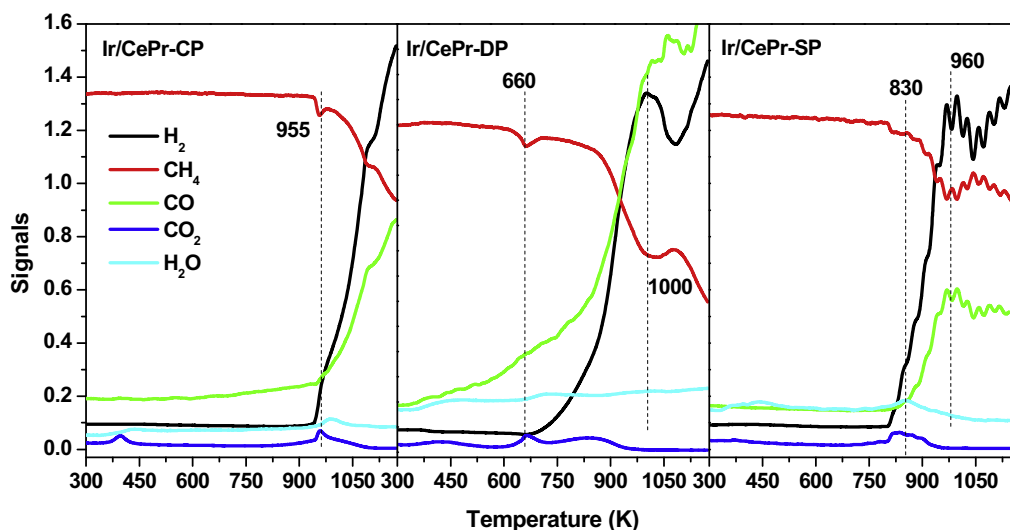**Fig. 7.** CH_4-TPSR profiles of the $Ir/Ce_{0.9}Pr_{0.1}O_2$ catalysts.

Fig. 8. TPSR of CH_4+CO_2 over the $Ir/Ce_{0.9}Pr_{0.1}O_2$ catalysts.

perature increases. At low temperatures, the reaction between CH_x and the active surface oxygen species occurs at the metal-support joint to yield CO_2 and H_2O. At high temperatures, CH_x reacts with the bulk oxygen species to produce syngas. The oxygen species in the catalysts could be compensated from the interaction between CO_2 and the mixed oxides.

### 3.4. Catalytic performances and stability tests of the $Ir/Ce_9Pr_{0.1}O_2$ catalysts

Fig. 9 presents the catalytic performances of DRM over the catalysts from 873 K to 1023 K. Both conversions of CH_4 and CO_2 were observed to progressively increase with the temperature. At 873 K, the CH_4 conversions are 32.7%, 16.1% and 13.4% over the catalysts prepared by DP, SP and CP, respectively. The corresponding values become 61.1%, 48.3% and 44.5% at 1023 K. In the case of CO_2, the conversions are 41.5%, 26.4% and 23.2% at 873 K over the $Ir/Ce_{0.9}Pr_{0.1}O_2$-DP, $Ir/Ce_{0.9}Pr_{0.1}O_2$-SP and $Ir/Ce_{0.9}Pr_{0.1}O_2$-CP catalysts, respectively, and increase to 74.5%, 68.7% and 61.9% at 1023 K. The H_2/CO product ratio exhibited high dependency on both the reaction temperature and the catalysts. Among the values, the low-

est one is about 0.39 over the $Ir/Ce_{0.9}Pr_{0.1}O_2$-CP catalyst at 873 K, and the highest one is about 0.97 over the $Ir/Ce_{0.9}Pr_{0.1}O_2$-DP catalyst at 1023 K. These data were agreed with the previous results [16].

From the analysis of catalysts preparation methods, it is derived that Ir is unembedded on the $Ir/Ce_{0.9}Pr_{0.1}O_2$-DP catalyst, but partially or fully embedded on the $Ir/Ce_{0.9}Pr_{0.1}O_2$-SP and $Ir/Ce_{0.9}Pr_{0.1}O_2$-CP catalysts. This difference may result in a higher CH_4 activation ability at Ir metal sites on the $Ir/Ce_{0.9}Pr_{0.1}O_2$-DP catalyst. Furthermore, the more active surface and bulk oxygen of the $Ir/Ce_{0.9}Pr_{0.1}O_2$-DP catalyst compared to those of the $Ir/Ce_{0.9}Pr_{0.1}O_2$-SP and $Ir/Ce_{0.9}Pr_{0.1}O_2$-CP catalysts also contributes to the higher performance. As to CO_2, the highest interaction with the $Ce_{0.9}Pr_{0.1}O_2$-DP support provides the highest CO_2 conversion over the $Ir/Ce_{0.9}Pr_{0.1}O_2$-DP catalyst.

Fig. 10 gives the results of stability tests at 1023 K. The conversions of CH_4 and CO_2, as well as the H_2/CO product ratio are not significantly varied during the testing hours. Although the conversions of CH_4 are all marginally decreased over the catalysts after 200 h on stream, the $Ir/Ce_{0.9}Pr_{0.1}O_2$-DP catalyst still maintained the highest catalytic performance. The higher performance of the
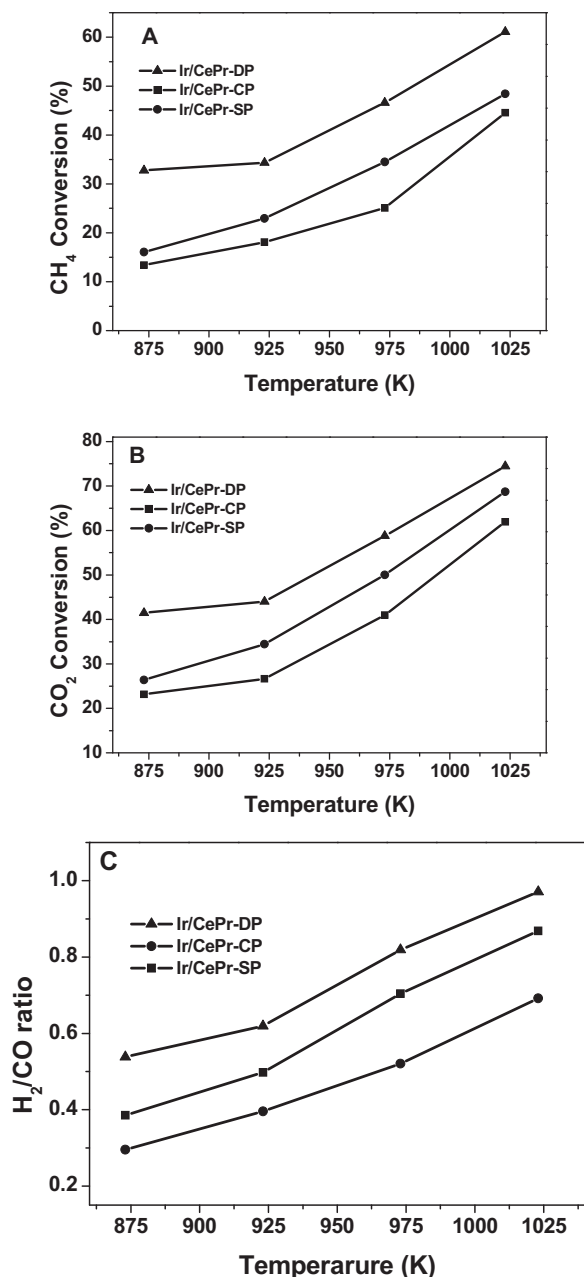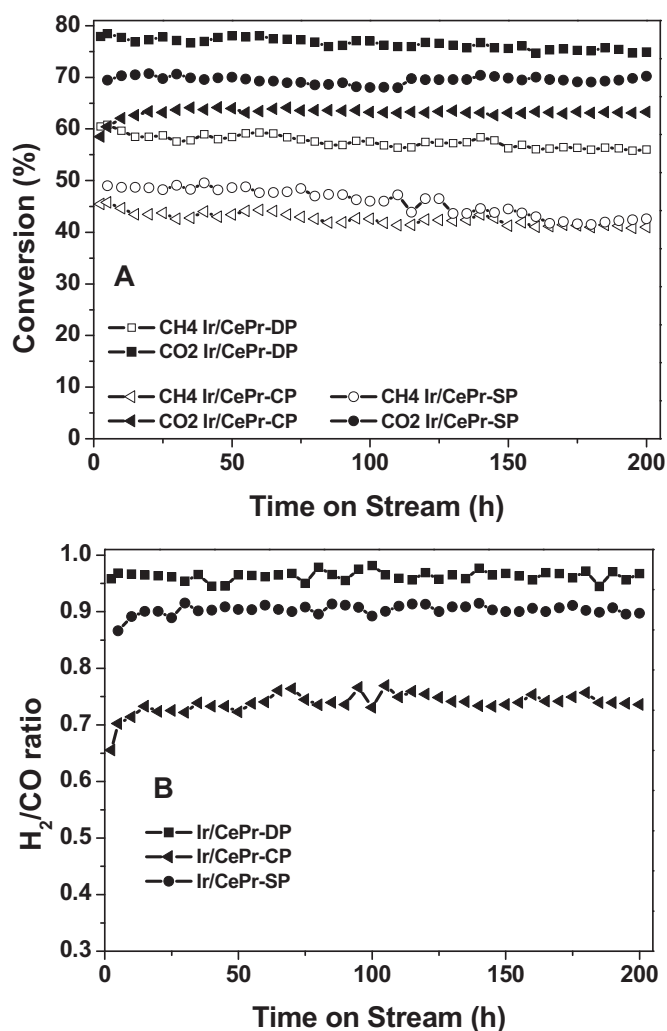
Fig. 9. Conversions of methane (A) and carbon dioxide (B), and H_2/CO product ratios (C) as a function of temperature from 873 to 1023 K over the $Ir/Ce_{0.9}Pr_{0.1}O_2$ catalysts. Reaction conditions: mass of catalyst: 100 mg, flow rate: $F_{CH4} = F_{CO2} = 15$ mL/min, GHSV = 18,000 mL/(gh), $P = 0.1$ MPa.

$Ir/Ce_{0.9}Pr_{0.1}O_2$-DP catalyst could be associated with the more basicity of mixed oxide to efficient active CO_2, the more accessible Ir nanoparticles to transform CH_4 and the Ir-support boundary to remove the coke precursors.

3.5. Intrinsic reaction rates over the $Ir/Ce_9Pr_{0.1}O_2$ catalysts

In order to further confirm the highest performance of the $Ir/Ce_{0.9}Pr_{0.1}O_2$-DP catalyst, intrinsic reaction rates of the three catalysts were measured at low conversion of CH_4 (less than 10%) and 773 K. The rates of CH_4 are 6.08, 1.77 and 4.80 $\mu mol/(g_{cat} \cdot s)$ over the $Ir/Ce_{0.9}Pr_{0.1}O_2$-DP, $Ir/Ce_{0.9}Pr_{0.1}O_2$-CP and $Ir/Ce_{0.9}Pr_{0.1}O_2$-SP, respectively. The trend agrees with that of catalytic performances as shown in Fig. 9. Again, the highest catalytic rate was obtained

Fig. 10. Stability tests of methane/carbon dioxide conversions (A) and H_2/CO product ratio (B) at 1023 K over the $Ir/Ce_{0.9}Pr_{0.1}O_2$ catalysts. Reaction conditions: mass of catalyst: 100 mg, flow rate: $F_{CH4} = F_{CO2} = 15$ mL/min, GHSV = 18,000 mL/(gh), $P = 0.1$ MPa, $T = 1023$ K.

over the $Ir/Ce_{0.9}Pr_{0.1}O_2$-DP catalyst, which could be attributed to the unembedded Ir on the $Ce_{0.9}Pr_{0.1}O_2$-DP surface that enhances the activation of CH_4 and promotes CH_x intermediates transformation by oxygen species at the metal-support boundaries.

3.6. Characterizations of the used $Ir/Ce_9Pr_{0.1}O_2$ catalysts after long time hours on stream

Table 1 also compares the texture properties of the used samples. Although the BET surface areas and the pore volumes of the catalysts are all suffered shrinkage after the long time stability tests, the BET surface area and the pore volume of the used $Ir/Ce_{0.9}Pr_{0.1}O_2$-DP catalyst were slightly higher than those of the other two catalysts, which will facilitate the mass transfer for the gaseous reactants. In the meantime, the sintering degree of mixed oxide was about 82% in the used $Ir/Ce_{0.9}Pr_{0.1}O_2$-DP catalyst, while were 107% and 114% in the used $Ir/Ce_{0.9}Pr_{0.1}O_2$-SP and $Ir/Ce_{0.9}Pr_{0.1}O_2$-CP catalysts, respectively. Hence the most severe sintering of support in the $Ir/Ce_{0.9}Pr_{0.1}O_2$-CP catalyst deduced the lowest catalytic performance. In contrast, the lightest sintering of support in the $Ir/Ce_{0.9}Pr_{0.1}O_2$-DP catalyst evidenced the best thermal stability and thus behaved the best catalytic activity and stability as shown in Fig. 10.

Fig. 11 shows the XRD patterns of the used $Ir/Ce_{0.9}Pr_{0.1}O_2$ catalysts. Characteristic diffraction lines of ceria without PrO_x species were observed, implying the retention of the solid solution structures of the mixed oxides. The crystalline sizes of the mixed oxides increase to 30 nm, 31 nm and 27 nm for the $Ir/Ce_{0.9}Pr_{0.1}O_2$ catalysts prepared by DP, CP and SP, respectively. This indicates the occurrence of sintering in the mixed oxides after long operation hours. The diffraction peak of Ir was observed in the $Ir/Ce_{0.9}Pr_{0.1}O_2$-DP catalyst, but was still undetectable in the $Ir/Ce_{0.9}Pr_{0.1}O_2$-CP and $Ir/Ce_{0.9}Pr_{0.1}O_2$-SP catalysts. These clearly suggest that extensive Ir sintering does not occur in the catalysts prepared by CP and SP, which might be attributed to the stronger metal-support interaction restricting the Ir movement. Combined the above results with the stability performances, it can be proposed that the slight decrease of performances may be associated with the sintering of the mixed oxides, which lessens the active surface oxygen and slows down the conversion rate of CH_x. TEM images of the used catalysts are illustrated in Fig. 12. For the $Ir/Ce_{0.9}Pr_{0.1}O_2$-DP catalyst (Fig. 12A and B), Ir nanoparticles with size about 5 nm are dispersed on the support with sizes of 20–30 nm. For $Ir/Ce_{0.9}Pr_{0.1}O_2$-CP catalyst (Fig. 12C and D), although the size of the mixed oxide was
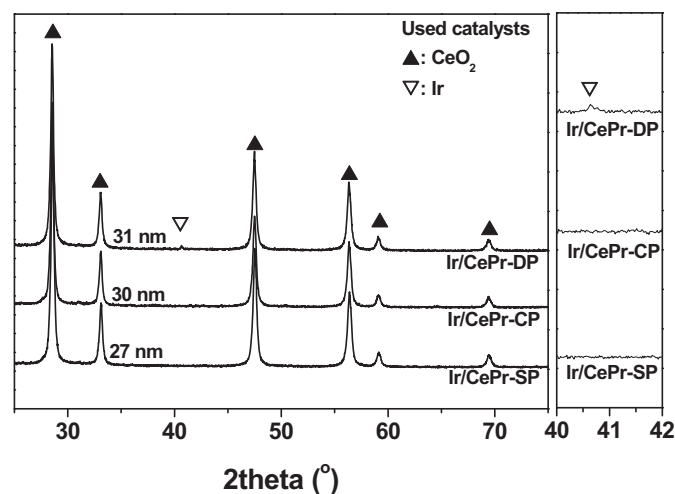

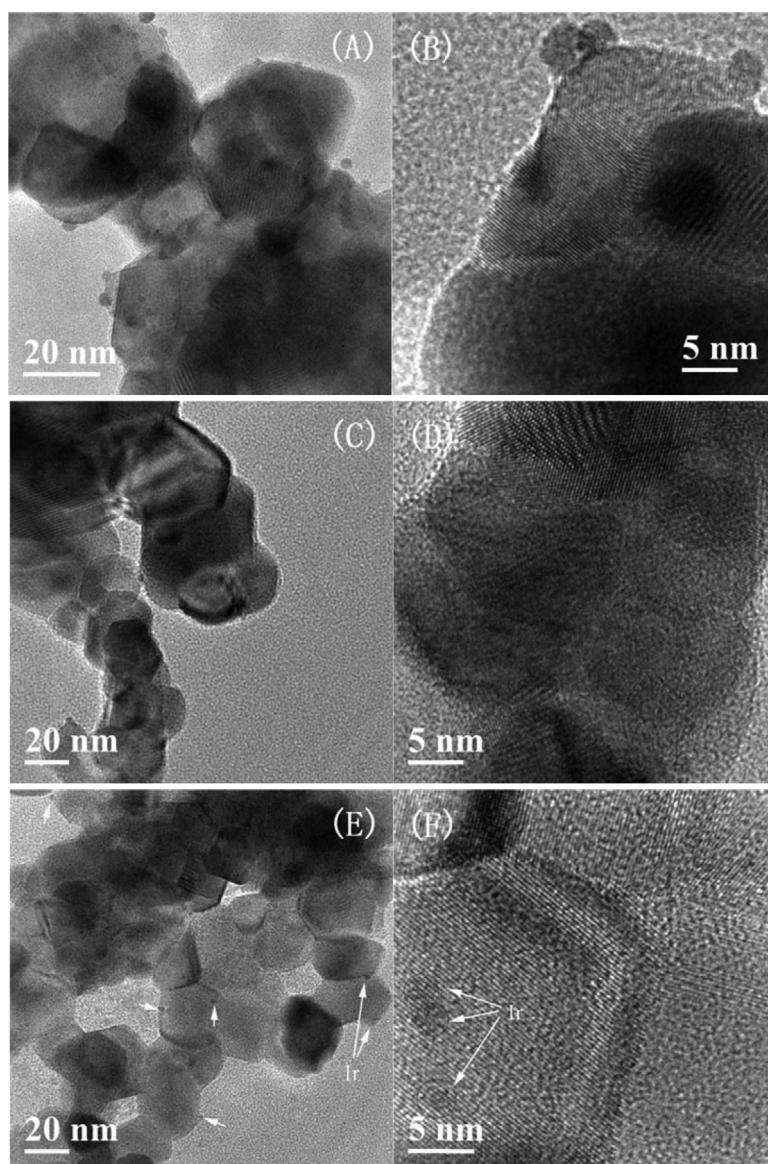**Fig. 11.** XRD patterns of the used $Ir/Ce_{0.9}Pr_{0.1}O_2$ catalysts after 200 h on stream.

Fig. 12. TEM images of used $Ir/Ce_{0.9}Pr_{0.1}O_2$ catalysts after 200 h on stream. (A and B: $Ir/Ce_{0.9}Pr_{0.1}O_2$-DP, C and D: $Ir/Ce_{0.9}Pr_{0.1}O_2$-CP, E and F: $Ir/Ce_{0.9}Pr_{0.1}O_2$-SP).
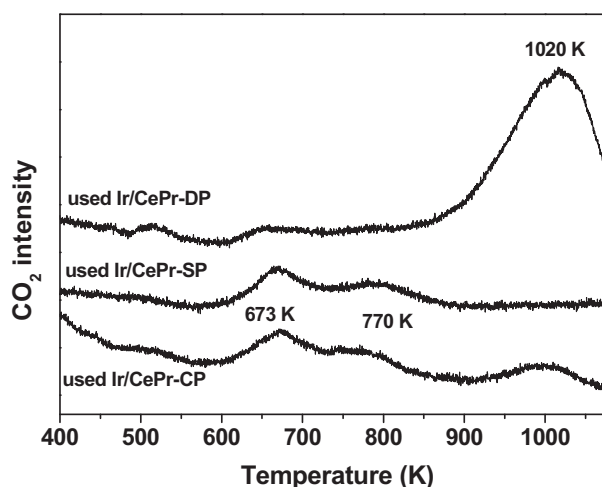
Fig. 13. TPO profiles of used Ir/Ce$_{0.9}$Pr$_{0.1}$O$_2$ catalysts.

increased to 30-40 nm, the Ir nanoparticles were hardly observed, indicating that the Ir species are still fully embedded in the mixed oxide. In the case of the Ir/Ce$_{0.9}$Pr$_{0.1}$O$_2$-SP catalyst (Fig. 12E and F), the formation of small Ir nanoparticles (2–3 nm) was observed on the surface in addition to the enlargement of mixed oxide particles. However, the density of the Ir nanoparticles is rather low compared to that on the Ir/Ce$_{0.9}$Pr$_{0.1}$O$_2$-DP catalyst. This observation may possibly suggest that partial embedment of Ir species in the matrix of the Ir/Ce$_{0.9}$Pr$_{0.1}$O$_2$-SP catalyst. No obvious carbon deposition can be seen on the used samples, which can be attributed to the high OSC of the catalysts in removing coke precursors.

TPO studies of the used catalysts (Fig. 13) were performed to verify the carbonaceous formation although they were not observed in the TEM images. In the TPO results, carbonaceous deposits were detected at 673–770 K and 1020 K over the Ir/Ce$_{0.9}$Pr$_{0.1}$O$_2$-CP catalyst, 673–770 K over the Ir/Ce$_{0.9}$Pr$_{0.1}$O$_2$-SP catalyst and 1020 K over the Ir/Ce$_{0.9}$Pr$_{0.1}$O$_2$-DP catalyst. It is suggested that at least two types of carbon deposits were formed on used catalysts. The peak at 673–770 K is related to amorphous carbon and the peak at 1020 K is associated with graphic carbon [14,27]. The amounts of deposits are only 0.32wt%, 0.30wt% and 0.53wt% on the Ir/Ce$_{0.9}$Pr$_{0.1}$O$_2$-CP, Ir/Ce$_{0.9}$Pr$_{0.1}$O$_2$-DP and Ir/Ce$_{0.9}$Pr$_{0.1}$O$_2$-DP catalysts, respectively. This negligible carbon deposits could be explained from the effective removal of carbon precursors at Ir-support boundaries. Hence stable catalytic performance was achieved although graphic carbon was deposited over the Ir/Ce$_{0.9}$Pr$_{0.1}$O$_2$-DP catalyst.

4. Conclusions

Novel Ir/Ce$_{0.9}$Pr$_{0.1}$O$_2$ catalysts were synthesized for DRM reaction. The locations of Ir species and the redox properties of the catalysts were adjusted by different preparation methods. The most unembedded Ir to activate methane and the active oxygen species to convert CH$_x$ intermediates results in the highest CH$_4$ conversion over the Ir/Ce$_{0.9}$Pr$_{0.1}$O$_2$-DP catalyst. The metal-support interaction limits the Ir sintering and the OSC prevents coke deposition.

The slight decrease of catalytic performances over the time can be attributed to the sintering of the mixed oxides during the catalytic process.

References

[1] D. Pakhare, J. Spivey, Chem. Soc. Rev. 43 (2014) 7813–7837.
[2] X. Guo, G. Fang, G. Li, H. Ma, H. Fan, L. Yu, C. Ma, X. Wu, D. Deng, M. Wei, D. Tan, R. Si, S. Zhang, L.S.J. Li, Z. Tang, X. Pan, X. Bao, Science 344 (2014) 617–619.
[3] A.A. Olajire, J. CO2 Util. 3–4 (2013) 74–92.
[4] M.G. Dieguez, I.S. Pieta, M.C. Herrera, M.A. Larrubia, L.J. Alemany, J. Catal. 270 (2010) 136–145.
[5] B. Bachiller-Baeza, C. Mateos-Pedrero, M.A. Soria, A. Guerrero-Ruiz, U. Rodemerck, I. Rodríguez-Ramos, Appl. Catal. B Environ. 129 (2013) 450–459.
[6] A.I. Paksoy, B.S. Caglayan, A.E. Aksoylu, Appl. Catal. B Environ. 168–169 (2015) 164–174.
[7] M.M. Nair, S. Kaliaguine, F. Kleitz, ACS Catal. 4 (2014) 3837–3846.
[8] A. Derk, G. Moore, S. Sharma, E. McFarland, H. Metiu, Top. Catal. 57 (2014) 118–124.
[9] P. Djinovic, J. Batista, A. Pintar, Int. J. Hydrogen Energy 37 (2012) 2699–2707.
[10] C. Liu, J. Ye, J. Jiang, Y. Pan, ChemCatChem 3 (2011) 529–541.
[11] A.T. Ashcroft, A.K. Cheetham, M.L.H. Green, P.D.F. Vernon, Nature 352 (1991) 225–226.
[12] J.R.R. Nielsen, J.H.B. Hansen, J. Catal. 144 (1993) 38–49.
[13] R. Wang, X. Liu, Y. Chen, W. Li, H. Xu, Chin. J. Catal. 28 (2007) 865–869.
[14] M. Rezaei, S.M. Alavi, S. Sahebdelfar, Z.F. Yan, J. Nat. Gas Chem. 15 (2006) 327–334.
[15] A.I. Tsyganok, M. Inaba, T. Tsunoda, S. Hamakawa, K. Suzuki, T. Hayakawa, Catal. Commun. 4 (2003) 493–498.
[16] M. Wisniewski, A. Boreave, P. Gelin, Catal. Commun. 6 (2005) 596–600.
[17] J.H. Bitter, K. Seshan, J.A. Lercher, J. Catal. 176 (1998) 93–101.
[18] H.C. Yao, Y.F.Y. Yao, J. Catal. 86 (1984) 254–265.
[19] S. Bedrane, C. Descorme, D. Duprez, Catal. Today 75 (2002) 401–405.
[20] F. Wang, W. Cai, H. Provendier, Y. Schuurman, C. Descorme, C. Mirodatos, W. Shen, Int. J. Hydrogen Energy 36 (2011) 13566–13574.
[21] J.A. Farmer, C.T. Campbell, Science 329 (2010) 933–936.
[22] G. Deganello, F. Giannici, A. Martorana, G. Pantaleo, A. Prestianni, J. Phys. Chem. B 110 (2006) 8731–8739.
[23] M. Cargnello, J.J.D. Jaen, J.C.H. Garrido, K. Bakhmutsky, T. Montini, J.J.C. Gamez, R.J. Gorte, P. Fornasiero, Science 337 (2012) 713–716.
[24] H. Li, G. Qi, T. Na, X. Zhang, X. Huang, W. Li, W. Shen, App. Catal. B Environ. 103 (2011) 54–61.
[25] S. Damyanova, B. Pawelec, K. Arishtirova, M.V.M. Huerta, J.L.G. Fierro, Appl. Cata. A Gen. 337 (2008) 86–96.
[26] B.M. Reddy, G. Thrimurthulu, L. Katta, Y. Yamada, S.E. Park, J. Phys. Chem. C 113 (2009) 15882–15890.
[27] W. Cai, F. Wang, C. Daniel, A.C.V. Veen, Y. Schuurman, C. Descorme, H. Provendier, W. Shen, C. Mirodatos, J. Catal. 286 (2012) 137–152.
[28] F. Wang, W. Cai, T. Na, H. Provendier, Y. Schuurman, C. Descorme, C. Mirodatos, W. Shen, App. Catal. B Environ. 125 (2012) 546–555.
[29] L. Li, L. Song, C. Chen, Y. Zhang, Y. Zhan, X. Lin, Q. Zheng, H. Wang, H. Ma, L. Ding, W. Zhu, Int. J. Hydrogen Energy 39 (2014) 19570–19582.
[30] M.D.S. Villalpando, D.A. Berry, T.H. Gardner, Int. J. Hydrogen Energy 33 (2008) 2695–2703.
[31] J.C. Lavalley, Catal. Today 27 (1996) 377–401.
[32] L.G. Appel, J.G. Eon, M. Schmal, Catal. Lett. 56 (1998) 199–202.
[33] K. Li, H. Wang, Y. Wei, J. Chem. 2013 (2013) 1–8.
[34] T.V. Choudhary, V.R. Choudhary, Angew. Chem. Int. Ed. 47 (2008) 1828–1847.
[35] X. Du, D. Zhang, L. Shi, R. Gao, J. Zhang, J. Phys. Chem. C 116 (2012) 10009–10016.